

Modeling of the driver transverse profile for laser wakefield electron acceleration at APOLLON Research Facility

I. Moulanier¹, L.T. Dickson¹, C. Ballage¹, O. Vasilovici¹, A. Gremaud¹, S. Dobosz Dufrénoy², N. Delerue³, L. Bernardi⁴, A. Mahjoub⁴, A. Cauchois⁴, A. Specka⁴, F. Massimo¹, G. Maynard¹, B. Cros¹

¹ *LPGP, CNRS, Université Paris Saclay, 91405 Orsay, France*

² *CEA, CNRS, LIDYL, Université Paris Saclay, 91190 Gif sur Yvette, France*

³ *IJCLAB, CNRS, Université Paris Saclay, 91405 Orsay, France*

⁴ *LLR, CNRS/IN2P3, Ecole Polytechnique, Institut Polytechnique de Paris, 91120 Palaiseau, France and*

**Corresponding authors : I. Moulanier, ioaquin.moulanier@universite-paris-saclay.fr; B. Cros, brigitte.cros@universite-paris-saclay.fr*

(Dated: May 11, 2023)

The quality of electron bunches accelerated by laser wakefields is highly dependant on the temporal and spatial features of the laser driver. Analysis of experiments performed at APOLLON PW-class laser facility shows that spatial instabilities of the focal spot, such as shot-to-shot pointing fluctuations or asymmetry of the transverse fluence, lead to charge and energy degradation of the accelerated electron bunch. It is shown that PIC simulations can reproduce experimental results with a significantly higher accuracy when the measured laser asymmetries are included in the simulated laser's transverse profile, compared to simulations with ideal, symmetric laser profile. A method based on a modified Gerchberg-Saxton iterative algorithm is used to retrieve the laser electric field from fluence measurements in vacuum in the focal volume, and accurately reproduce experimental results using PIC simulations, leading to simulated electron spectra in close agreement with experimental results, for the accelerated charge, energy distribution and pointing of the electron beam at the exit of the plasma.

I. INTRODUCTION

In the process of Laser WakeField Acceleration (LWFA) [1, 2], an ultra-high intensity laser is focused inside a gas target, ionizes the medium and creates a trailing perturbation in its wake in an underdense plasma. The generated plasma cavity sustains intense longitudinal and transverse electric fields that can trap, accelerate and focus bunches of electrons to the GeV range [3] within a few centimeters. Injection of plasma electrons makes LWFA a compact option for the generation of relativistic electron sources. However, despite numerous studies, the use of electron beams from LWFA for applications is impeded by insufficient beam quality and stability. Therefore, detailed diagnostics, realistic modeling and analysis are needed to achieve a precise understanding of the key mechanisms controlling the laser plasma interaction in experiments.

The main schemes for the injection of plasma electrons into the plasma wave are self-injection [4] and ionization injection [5–8]. In LWFA experiments with PW-class laser drivers, both injection schemes can occur in the so-called bubble regime [9], in which the ponderomotive force of the laser repels plasma electrons from its propagation axis, generating an electron-free cavity behind the laser pulse. In the process of self-injection, a portion of the expelled plasma electrons travel around the cavity before getting trapped in the wakefield [10]. In ionization injection, the gas target is a mixture of light atomic species, typically hydrogen, ionized early before the peak

of the laser pulse, and a dopant species, e.g. nitrogen, presenting an energy-gap in its ionization potential structure [7], leading to ionization of some electrons close to the peak of the laser pulse.

With peak intensities above $I_0 = 10^{18}$ W/cm², the pulse temporal front ionizes hydrogen and nitrogen up to N^{5+} . Remaining nitrogen L-shell electrons are primarily born around laser peak intensities, inside the bubble [11]. Ionization injection has several properties of interest for tuning electron injection and trapping, and favors highly charged electron beams. It operates at an intensity below self-injection [8] and the two mechanisms can be optimized in different parameter areas. As ionization injection depends on the local intensity of the laser pulse, it can be particularly sensitive to laser beam quality and its evolution during propagation in the evolving plasma density. These properties can be used to control the injection process in electron density tailored profile or diagnose laser beam quality.

The electron beam charge can be increased by increasing the driving laser power, providing a large range of parameters to explore for optimizing the properties of laser driven electron sources with PW class short pulse laser facilities.

This complex nonlinear physics is described using particle in cell (PIC) simulations [12], using as input parameters the laser temporal and spatial shapes, and the gas density profile. Experimentally achieved laser beams often differ from perfectly symmetrical distributions. Hence, in order to understand the role of laser imperfections on the quality of the produced electron bunches, and compare to experimental results, refined

PIC simulations describing realistically the injection and acceleration physics occurring at the ps scale were performed. These realistic simulations require a proper description of the gas density profile, as well as of the driver (laser profile transverse asymmetries) to accurately reproduce laser-plasma interactions affecting the electron beams characteristics. For instance, laser asymmetries have been shown to lead to asymmetric wakefields affecting the output accelerated electron beam, with characteristics directly correlated with the laser stability and quality [13–17].

In this paper the method used to analyze characteristic results obtained during commissioning experiments at APOLLON PW facility [18] is presented. Focusing the F_2 laser beam at 0.4 PW in the long focal area inside a gas cell [19], experiments were performed to characterize laser beam quality and evaluate its impact on electron properties.

It is shown that PIC simulations can reproduce experimental results with a significantly higher accuracy when the measured laser asymmetries are included in the simulated laser's transverse profile. This enhanced agreement is meant in comparison with simulations with an ideal, axisymmetric laser profile, which is often used in the design stage of LWFA experiments and in preliminary experimental analyses. The results described in this work thus show the importance of more realistic initial conditions in numerical modeling used for these studies. The simulation results shown in this work were obtained with the quasi-3D PIC code FBPIC [20], but the same method can be applied with other PIC codes in quasi-3D [21] or full 3D geometry.

In comparison to previous investigations made with realistic PIC simulations in [14], this work uses an alternative fast Gerchberg-Saxton algorithm [22] based on mode decomposition to reconstruct the laser field, which allows the accurate simulation of an experimental electron bunch spectrum in the energy-angle plane. This method has already been used to present experimental results in [15], in a regime with a lower peak laser intensity and characterized by a more stable transverse laser profile from shot-to-shot. In addition, in this work, the physical effects of the realistic laser driver (in particular its asymmetries) on the electron injection in the bubble are described. An agreement between realistic numerical modeling and experiment is obtained also in the electron beam spectra in the energy-angle plane. Furthermore, the realistic simulations in [14] have been performed in 3D, while the realistic simulations of this work were performed in quasi-3D geometry [21], highlighting that high-fidelity simulations can be obtained also with this less computationally-demanding technique for preliminary analyses.

The remainder of this paper is organized as follows. Characteristic experimental results are presented in section II. The method used to retrieve the laser electric field from experimentally recorded fluence images is described in section III, followed by the description of the method

to generate data to initialize FBPIC simulations. A comparison of experimental and numerical electron spectra is discussed in section IV.

II. EXPERIMENTAL RESULTS

An experiment was performed in April 2021 during the commissioning phase of the long focal area of APOLLON facility to characterize laser beam quality inside the experimental area and evaluate its impact on electron beam quality.

After compression, the F_2 laser beam was transported into the experimental area and focused in vacuum using an on-axis spherical mirror 3 m focal length, after reflection from a turning mirror with a hole, as illustrated in Fig. 1.

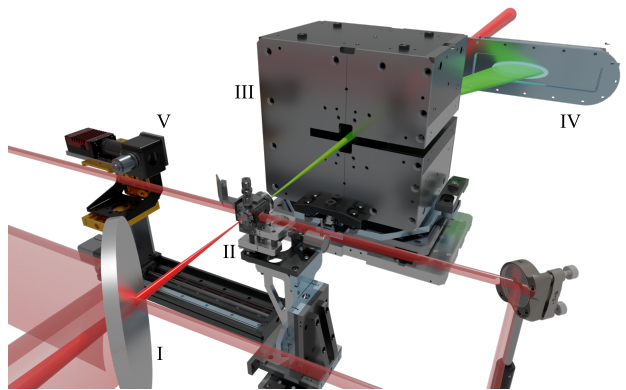


FIG. 1 : Schematic of experimental set-up : the driver laser beam (in red) is focused through the turning mirror (I) at the entrance of the gas cell (II), generating a diverging electron bunch (in green) at the exit. The electron bunch is then deflected by a magnetic dipole (III) and sent onto a LANEX screen (IV) to measure its Energy-Angle distribution. A small percentage of the laser driver is used to probe the plasma density transversely. Vacuum imaging of the focal volume is completed with a CCD (V).

The central part of the laser beam incident on the turning mirror was collected and used partly to monitor the laser beam energy from shot-to-shot using a leak through a wedge and a calorimeter. The remainder of the laser beam was used as a probe laser to diagnose plasma density transversely to the main pulse. The relative probing time was controlled by an in vacuum delay stage.

For this experiment, the APOLLON F_2 Ti : Sa laser with a central wavelength $\lambda = 0.8$, μm was measured to deliver a pulse with a FWHM intensity duration $\tau_{FWHM} = 25$ fs, a post-compression energy $E_l = 5$ to 10 J, with a repetition rate of 1 shot per minute. The peak intensity estimated in the ideal Gaussian transverse profile approximation in vacuum is 5×10^{19} W/cm². The laser beam was focused inside a 6 mm long gas cell [19] filled with a mixture of 99% H_2 and 1% N_2 . Electrons

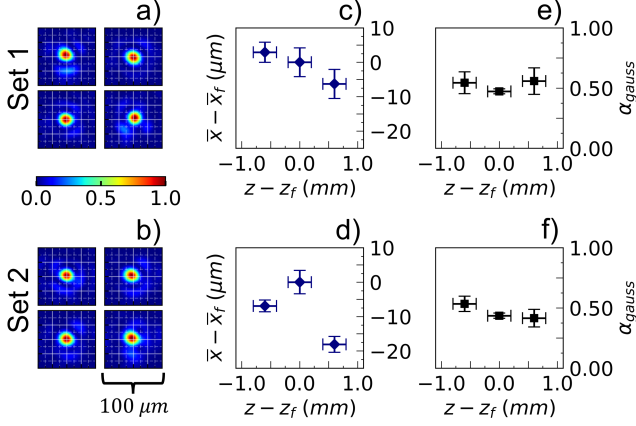


FIG. 2 : Measured laser beam stability during 2 sequences of multiple vacuum shots taken on 2 separate days with laser settings 1 and 2: (a) and (b) laser fluence of 4 consecutive shots measured in the focal plane; (c) and (d) $\bar{x} - \bar{x}_f$, laser beam relative centroid in the xOz plane, with respect to the focal plane centroid, for three positions $z - z_f$ along the laser propagation axis; the data for $z = z_f$ is from the 4 fluence images of (a) and (b), while the other points are data collected from 2 separate shots at each position; (e) and (f) fraction of energy α_{gauss} inside a Gaussian fit of waist w_0 . Error bars along z come from the determination of the focal plane z_f .

were trapped through ionization and accelerated in the wakefield. After plasma exit, their energy was measured using a dipole magnet and LANEX screen imaged onto a CCD camera. The spectrum was recorded in the 300 – 900 MeV energy range within a ± 20 mrad viewing angle.

The laser beam was characterized in detail in the focal volume every day prior to shots on the gas-filled target. Using a movable CCD camera in vacuum, the laser energy distribution was measured inside the interaction chamber before, at and after focus. The Rayleigh length in vacuum, defined as $z_R = (\pi w_0^2)/\lambda$, with w_0 being the $1/e^2$ radius of the focal plane intensity, was $z_R = 1$ mm. The waist of a Gaussian best fit in the focal plane is $w_0 = 16.6 \pm 0.3$ μm. Fig. 2 shows 2 sets of data taken on two different days, illustrating instabilities both in laser pointing and in spatial fluence symmetry between consecutive shots and for different days. Fig. 2.(a) and (b) show the fluence distribution in the focal plane $z = z_f$.

Fig. 2.(c) and (d) show the shot-to-shot transverse centroid displacement fluctuations $\bar{x} - \bar{x}_f$ in the focal volume (vertical error bars). The horizontal error bars come from the determination of the focal plane z_f . The xOz plane is the plane where electrons centroid fluctuations have been measured, perpendicularly to the laser polarization plane yOz . Fig. 2.(c) and (d) underline instabilities of the laser centroid in both cases. For Set 1 data the centroid is moving linearly, going from $+3$ μm at $z - z_f = -0.6$ mm to -6 μm at $z - z_f = +0.6$ mm. Set 2 data show larger fluctuations $\bar{x} - \bar{x}_f = -7$ μm at $z - z_f = -0.6$ mm and $\bar{x} - \bar{x}_f = -18$ μm at $z - z_f = +0.6$ mm. Multi-

directional fluctuations of the centroid around the focal plane are the signature of a non zero temporal phase and the asymmetry of the laser fluence.

In Fig. 2.(e) and (f), α_{gauss} , defined as the fraction of total energy inside a Gaussian fit with waist w_0 , is plotted as a function of position in the focal volume. Values of α_{gauss} at $z \neq z_f$ are calculated using a waist $w(z) = w_0[1 + (z/z_R)^2]^{1/2}$ for the Gaussian fit. At $z = z_f$, α_{gauss} is averaging 46 % for Set 1 and 40 % for Set 2. This demonstrates that the experimental fluence departs significantly from a perfect Gaussian approximation in both cases.

Figure 3 shows the average of 10 consecutive electron bunch spectra measured on the same day as Fig. 2 Set 1, in yOx , also defined as the $Energy - \theta_x$ angle plane. The average bunch charge measured between 300 and

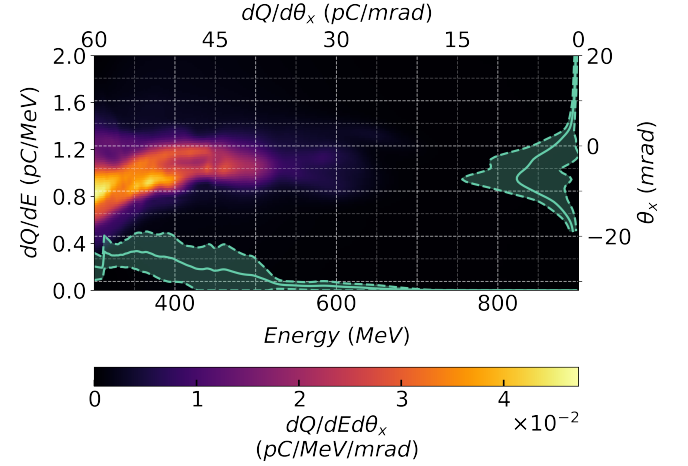


FIG. 3 : Average electron spectrum of 10 consecutive shots acquired the same day as Fig. 2 Set 1 laser measurements for an average plasma electron density $\bar{n}_0 = 2.2 \times 10^{18}$ cm $^{-3}$. The color scale shows the spectral charge density in the $Energy - \theta_x$ angle plane. The full green line along the $Energy$ axis is the average spectral charge density, dQ/dE , profile (scale on left vertical axis) calculated within ± 3 mrad around each individual maximum $dQ/d\theta_x$. The full green line along the θ_x axis (right-hand side vertical axis) represents the average $dQ/d\theta_x$ profile (scale on the top horizontal axis) integrated over energy. The green areas are the confidence intervals bounded by the standard deviation extremes (dashed curves). $\theta_x = 0$ corresponds to the laser axis alignment position in vacuum.

900 MeV and within ± 20 mrad is $\bar{Q}_{tot} = 95 \pm 46$ pC. For this sequence, the mean measured laser energy is $\bar{E}_l = 4.8 \pm 0.2$ J, and average plasma electron density $\bar{n}_0 = 2.2 \pm 0.2 \times 10^{18}$ cm $^{-3}$. The measured charge fluctuations are $\delta\bar{Q}_{tot}/\bar{Q}_{tot} = 47$ %, which shows a clear sensitivity to input parameters.

III. MODELING OF THE LASER BEAM

The analysis and implementation of the laser experimental data into PIC simulations are performed in three steps. First, the laser electric field is retrieved from the measured fluence data. Then, the reconstructed laser electric field is represented as a mode sum of fields that are used as parameters at the start of PIC simulations. Finally, the calculated electron parameters at the end of each simulation are compared with measured results.

A. Fit of the laser electric field

A modified version of the reconstructive Gerchberg-Saxton algorithm (GSA) [22], described in Appendix A, was used to retrieve the laser electric field corresponding to the laser fluence measured at 3 positions : $z - z_f = 0, +1.2, -1.8$ mm.

The algorithm was used in particular to retrieve an unknown phase map, $\psi(x, y)$, associated to a set of fluence images measured at different positions ($z_0, z_1 \dots z_{k_{max}}$).

We selected laser data from the same day as Fig. 2 Set 1, which exhibit better focal spot stability than Set 2, to reconstruct a realistic laser electric field distribution. For each position, the corresponding fluence distribution has been re-centered around the origin in order to reduce in advance the shot-to-shot fluctuations error on the fit. The selected experimental distributions (upper row) and results of the fit algorithm (middle row) are plotted in Fig. 4.

Using a combination of low order fits to establish an educated guess, then refining the optimization with a higher order Hermite-Gaussian modes projection, a realistic reconstructed distribution is calculated as represented in Fig.4, (middle row).

The laser fluence reconstructed with Laguerre-Gauss modes is plotted in Fig. 4 (lower row) and shows a relatively good agreement between the reconstructed Laguerre-Gauss distribution and the experimental laser data.

B. PIC simulation set-up

Due to the cylindrical representation used in FBPIC, the reconstructed Hermite-Gauss laser electric field $E_{HG}(r, \theta, z_f)$ is projected on Laguerre-Gauss modes [23] in the focal plane $z = z_f$:

$$C_{l,m} = \int_{r=0}^{r_{max}} \int_{\theta=0}^{2\pi} r dr d\theta E_{HG}(r, \theta, z_f) \times LG_{l,m}^*(r, \theta, z_f)(r, \theta, z_f, r_{0,opt}, \theta_{0,opt}, w_{0r}) \quad (1)$$

with $C_{l,m}$ being the complex amplitudes of the $LG_{l,m}$ Laguerre-Gauss modes, l the azimuthal order, m the radial order, $*$ the complex conjugate operator, $w_{0r} =$

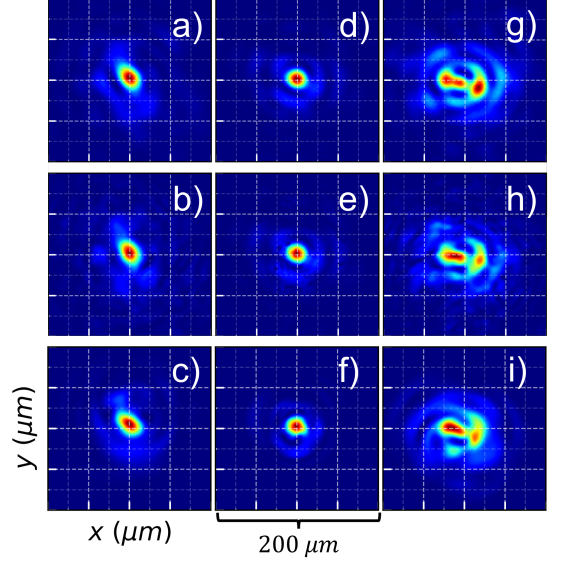


FIG. 4 : Experimental laser fluence measured in the focal volume (upper row), corresponding Hermite-Gaussian reconstruction (middle row), Laguerre-Gauss fit with $L = 3$ and $M = 40$ used in simulations (lower row): (a), (b) and (c) $z - z_f = -1.8$ mm - (d), (e) and (f) $z - z_f = +0$ mm - (g), (h) and (i) $z - z_f = +1.2$ mm. Each distribution has been normalized by its peak fluence.

$(w_{0x}^2 + w_{0y}^2)^{1/2}$ the projection waist, $(r_{0,opt}, \theta_{0,opt})$ the GSA cycle optimized origins in cylindrical coordinates at $z = z_f$ and $r_{max} = \min(\Delta X/2, \Delta Y/2)$. The rectangular grid length along each axis is denoted by $(\Delta X, \Delta Y)$.

For a given number M of radial modes, the quality of the Laguerre-Gauss projection as a function of the number of azimuthal modes taken into account (azimuthal order L) is evaluated by calculating ϵ_{fit} , the integral error, defined as :

$$\epsilon_{fit} = \frac{\int_{r=0}^{r_{max}} \int_{\theta=0}^{2\pi} r dr d\theta |F_{HG}(r, \theta, z_f) - F_{LG}(r, \theta, z_f)|}{\int_{r=0}^{r_{max}} \int_{\theta=0}^{2\pi} r dr d\theta F_{HG}(r, \theta, z_f)} \quad (2)$$

with $F_{LG}(r, \theta, z_f)$ being the normalized fluence of the Laguerre-Gauss modes, $F_{HG}(r, \theta, z_f)$ the normalized fluence of the Hermite-Gauss modes from the laser electric field fit, both in the focal position $z = z_f$.

The integral error ϵ_{fit} decreases with the integration radius r_{max} for a fixed set of LG modes. ϵ_{fit} was calculated for an effective interaction radius, r_{eff} , to evaluate the quality of the Laguerre-Gauss fit near the peak fluence of the reconstructed profile. As injection and acceleration of electrons both occur within a characteristic radius around the laser centroid, on a scale of the order of the bubble radius $R_b \propto w_0$ [24], we set $r_{eff} = R_b$ and evaluate the error for $r \leq r_{eff}$ to measure the accuracy of the fit. In PIC simulations performed with a perfect Gaussian laser, the plasma cavity has values of R_b ranging from 15 to 20 μm . Therefore, we set $r_{eff} = 20 \mu m$ as

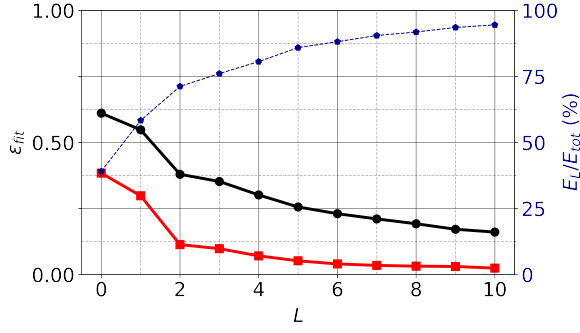


FIG. 5 : Integral error ϵ_{fit} for $M = 40$ radial modes, as a function of the maximum number of azimuthal modes L . Red squares: ϵ_{fit} calculated in a disk of radius $r_{eff} = 20 \mu\text{m}$; black circles: ϵ_{fit} calculated in a disk of radius $r_{max} = 200 \mu\text{m}$; blue diamonds (vertical axis on the right): cumulative energy fraction included in each configuration.

the value corresponding to the maximum observed bubble radius.

Figure 5 shows the evolution of ϵ_{fit} for $M = 40$ and L ranging from 0 to 10. The error of the fit converges toward $\epsilon_{fit} = 0$ both within r_{eff} and $r_{max} = 200 \mu\text{m}$ as the number of azimuthal modes used for projection increases. A share of 43% of the total energy is contained within the first mode $L = 0$ within a radius r_{eff} , which shows that the remainder is contained within non-symmetrical azimuthal modes.

The number of azimuthal modes for the Laguerre-Gauss harmonics needs $N = 5$ azimuthal modes to be simulated with the azimuthal harmonics of type $\exp\{-in\theta\}$ used in quasi-3D geometry [21]. In addition, the number of macro-particles per cell in the simulations in this work has been increased with the number of azimuthal modes to maintain a constant signal to noise ratio (whose value in quasi-3D simulations is discussed in [21]). As a result, the computational time required for a simulation with a Laguerre-Gauss laser field is increased due to the increased number of modes and of macro-particles per cell. Every simulation in this work with a Laguerre-Gauss sum laser profile used $L = 3$ and $M = 40$, which reproduces 75% of the total energy as shown in Fig. 5. For $L > 3$, the fit error ϵ_{fit} decreases slowly compared to the increase in computational time associated with the corresponding number of modes.

All numerical results presented in this paper were obtained with input parameters in the same range as those of the data shown in Fig. 3. The simulated laser beam has a FWHM duration $\tau_{FWHM,sim} = 25$ fs (Gaussian temporal profile) and the focal plane fluence is fitted with a Gaussian waist $w_{0,sim} = 16 \mu\text{m}$. The laser is propagated over 10 mm in a gas cell filled with 99% H_2 – 1% N_2 gas, including a starting 1.4 mm up-ramp from $n = 0$ to a density plateau of $n = n_{0,sim}$, as well as a down-ramp to $n = 0$ from $ct = 7.4$ mm to $ct = 10$ mm. The plasma density longitudinal profile profile is inferred from OpenFOAM simulations [19]. For both Gaussian and realistic

simulations, the laser driver is focused onto the start of the density plateau at $z_f = 1.4$ mm.

For simulations using the Gaussian profile, the energy was fixed at $E_{l,sim} = \alpha_{gauss} \times E_l$, with $\alpha_{gauss} = 0.46$ the value calculated in Fig. 2(e) at $z = z_f$. For simulations using the Laguerre-Gauss profile, simulated with $L = 3$ and $M = 40$, $E_{l,sim} = 0.75 \times E_l$.

The simulation grid is represented along z by $N_z = 3000$ points with an increment $\Delta z = 0.025 \mu\text{m}$, and along r by $N_r = 1100$ points with an increment $\Delta r = 0.2 \mu\text{m}$.

In the simulations with the reconstructed laser field profile, each population of H_2 and N_2 was simulated with $[P_z, P_r, P_\theta] = [2, 2, 16]$ macro-particles per cell along z , r and θ respectively. In the following, these simulations will be referred to as "realistic simulations".

Instead, every simulation using a perfect Gaussian laser profile was performed with $N_m = 2$ azimuthal modes. For these simulations, each population of H_2 and N_2 was simulated with $[P_z, P_r, P_\theta] = [2, 2, 4]$ macro-particles per cell.

IV. REALISTIC PIC SIMULATIONS RESULTS

A. Influence of laser asymmetry on electron beam spectra

To understand the physical impact of laser asymmetry on the electron bunch quality, realistic simulations were performed with FBPIC using the reconstructed laser driver retrieved from fluence distributions shown in Fig. 4. Input parameters were set as described in the previous section, and the electron density was fixed to $n_{0,sim} = 2.1 \times 10^{18} \text{ cm}^{-3}$.

For the sake of comparison between simulation and experimental results, 5 electron spectra are shown in Fig. 6: (a) simulation with a Gaussian laser driver, (b) simulation with a Laguerre-Gauss laser driver using distribution described by Figs. 4 and 5, both with electron density $n_{0,sim} = 2.1 \times 10^{18} \text{ cm}^{-3}$, and (c) to (e) experimental spectra (single instances of the data shown in Fig. 3) measured with electron densities $n_0 = 2.1 \times 10^{18} \text{ cm}^{-3}$ for (c) and (e), $n_0 = 2 \times 10^{18} \text{ cm}^{-3}$ for (d) and laser energy $E_l = 4.7$ J for (c) to (e). The total charge of the average of the experimental spectra from (c) to (e) is 111 pC, and their average central divergence is -6.6 mrad.

These results show that a Gaussian driver Fig. 6.(a) gives rise to a wide, high-energy, high-charge electron spectrum, peaked spatially on the laser axis. Using a realistic laser driver generates an off-axis electron beam with lower energy, lower charge, a structure in agreement with experimental results as shown in Fig. 6.(b) and (c) to (e), where all these spectra exhibit an off-axis $dQ/d\theta_x$ profile centered toward negative values. The final spectrum contains 20 % (0 %) of self-injected electrons for the Gaussian case (realistic cases).

Table I provides quantitative data for comparison

Spectrum	Q_{tot}	$\theta_{x,max}$	Peak Label	E_{peak}	$\Delta E_{peak}/E_{peak}$	Q_{peak}	$dQ/dE max.$
Units	pC	mrاد		MeV	%	pC	pC/MeV
Simulation Gauss	174	-0.3	1	556	3.2	7	0.38
			2	629	3.3	8	0.41
Simulation Laguerre-Gauss	109	-4.7	1	466	23.2	18	0.23
			2	632	8.6	5	0.11
Experimental Data	96	-3.8	1	424	20.3	17	0.21
			2	653	9.8	5	0.10

TABLE I : Comparison of electron properties retrieved from simulated (with ideal Gaussian and reconstructed laser profile) and experimental $\theta_x - E$ spectra shown in Fig. 6. Q_{tot} is the total charge on each Fig. 6 spectrum, $\theta_{x,max}$ the central divergence of the angular distribution, while the "peak" labelled quantities refer to the dQ/dE profiles that result from selection of $dQ/dE d\theta_x$ within a ± 3 mrad range around the maximum $dQ/d\theta_x$. Boldface denotes specific peak labels identified in Fig. 6 (a)-(c) dQ/dE profiles. $\Delta E_{peak}/E_{peak}$ is the energy spread FWHM for each peak, Q_{peak} is the FWHM charge contained within each peak and $dQ/dE max.$ is the maximum dQ/dE value reached within each peak.

of electron beam properties for the 3 cases shown in Fig. 6.(a) to (c). The total charge Q_{tot} is summed between ± 20 mrad and 300 – 900 MeV. We define the exit angle $\theta_{x,max}$ as the angle at which the maximum $dQ/d\theta_x$ is reached. Within ± 3 mrad, peaks with center energy E_{peak} , FWHM width $\Delta E_{peak}/E_{peak}$, and FWHM charge Q_{peak} , are identified based on minimum peak prominence $\delta_{dQ/dE} = 0.05$ pC/MeV and minimum base to base width $\delta_E = 45$ MeV. Values of Table I show that the results of the simulation with reconstructed laser field profile are in good agreement with the detailed electron beam structure measured in experiment, while the Gaussian simulation results in electron beam characteristics significantly different from the measured ones. Two major differences are Q_{tot} value, which is 45 % higher than the experimental data for the Gaussian case, and the overall dQ/dE structure which has a highest peak energy of 875 MeV against 653 MeV in the experimental data. The charge difference stems from the quality of the laser angular intensity profile as it is the only input difference between Gaussian and Laguerre-Gauss simulations.

The analysis of the evolution of laser symmetry during the propagation coupled to electron injection is discussed in the next section.

B. Evolution of the laser asymmetry and effects on electron dynamics

Figure 7 shows the simulated evolution of the laser beam and electron bunch characteristics in the xOz plane for the case with ideal Gaussian laser profile (left-hand column) and the case with the reconstructed laser field (right-hand column). It can be inferred from Fig. 7 that the evolution of laser asymmetry and maximum field amplitude define the conditions for electron injection and the dynamics of electrons during the acceleration process in the plasma cavity.

Figures 7.(a) and (b) show the evolution of the laser driver in the plasma density profile. As the realistic simulated transverse distribution is asymmetric with respect to the focal plane and changes before and after $z = z_f$ [Fig. 4], different spatial distortions occur during non-linear self-focusing inside the plasma.

To quantify the deviation from cylindrical symmetry of the transverse fluence $F(r, \theta)$ and track its evolution throughout the simulated propagation, we define an asymmetry coefficient σ_l [15] as :

$$\sigma_l = \int_{r=0}^{r_{max}} r dr \sqrt{\int_{\theta=0}^{2\pi} (d\theta (f(r, \theta) - \bar{f}(r)))^2}, \quad (3)$$

where the normalized laser fluence $f(r, \theta)$ is defined as

$$f(r, \theta) = \frac{F(r, \theta)}{\int_{r=0}^{r_{max}} \int_{\theta=0}^{2\pi} r dr d\theta F(r, \theta)}, \quad (4)$$

and $\bar{f}(r)$ is the mean normalized fluence over θ . The integral origin $r = 0$ is defined as the position of the fluence maximum. By definition, σ_l converges toward 0 for a cylindrically symmetric fluence profile.

This asymmetry coefficient σ_l is plotted for the Gaussian laser profile and realistic laser profile in Fig. 7.(a) and (b) respectively as a function of position along propagation axis. Figure 7.(a) confirms that the Gaussian profile is angularly symmetric. In this ideal case σ_l undergoes variations between $0.5e-5$ and $2.5e-5$. In comparison, its variations in the simulation with realistic laser field profile are on a scale 10^2 times larger. In the realistic case (Fig. 7.(b)), the amplitude of the symmetry coefficient drops by 67 % between 600 and 2000 μm , the focal plane in the plasma being in the middle of this area. This reduction of σ_l is simultaneous with the increase in a_0 , showing that tight focusing of the laser reduces its imperfections. In the realistic case, a_0 reaches values similar to the Gaussian

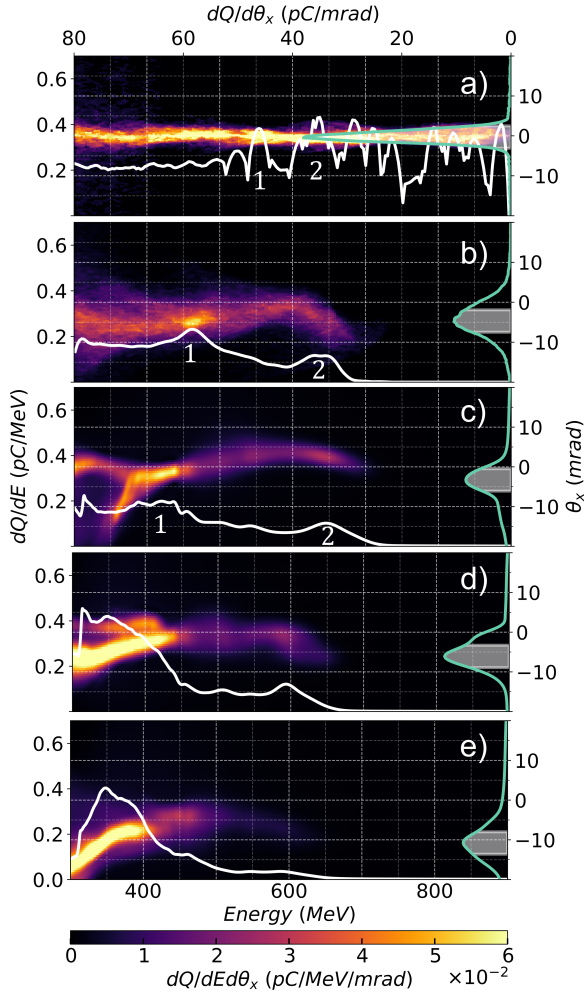


FIG. 6 : Electron bunch $dQ/dEd\theta_x$ spectral density in the energy θ_x divergence plane for 3 different cases : (a) simulated Gaussian spectrum - (b) simulated Laguerre-Gauss spectrum - (c) to (e) single experimental spectra from Fig. 3.(a) sequence. White (green) lines represent spectral charge, dQ/dE , (divergence charge density $dQ/d\theta_x$) integrated over the divergence (energy) respectively. The shaded area under the green $dQ/d\theta_x$ line shows the range ± 3 mrad around the peak of $dQ/d\theta_x$, used to produce the dQ/dE curve and calculate the spectrum peaks properties. The label 1 and 2 reference specific peaks within the dQ/dE profiles corresponding to Table I.

a_0 through the first self-focusing due to a near Gaussian shape in its focal plane (Fig. 4.(d)). However, the asymmetry of the intensity around the focal plane and relatively short typical variation length ($z_R = 1$ mm) are responsible for a 1 mm shift of the maximum in comparison to the Gaussian symmetric pulse [Fig. 7.(a) and (b)].

Figures 7.(c) and (d) show line profiles of injected charge Q_{inj} (right hand-side vertical axis), and spectral charge density $dQ/dE_{end}dz$ of electrons (black-red-yellow histogram) with final energy E_{end} , as functions of injection position z . In other words, this spectrum describes

distribution of the initial z positions of electrons for given final energies E_{end} .

The simulation with ideal Gaussian laser profile [Fig. 7.(c)] shows a correlation between final energy and injection position as electrons trapped earlier gain more energy over the interaction distance. The injection of electrons in ± 3 mrad around axis (green line) occurs inside a $400 \mu\text{m}$ window centered around the maximum laser amplitude a_{max} at $ct_1 = 1800 \mu\text{m}$. The green injected charge in this region (Fig. 7.(c)) is maximal because the process occurs over $0.4z_R$ within the density plateau, in the portion where $a_0 \simeq a_{max}$. Electrons injected at the start of this region see a longer accelerating length than the ones at the end, which results in decreasing final energy depending on the injection position. The resulting spectrum is evenly spread between 300 and 900 MeV as observed in Fig. 6.(a).

For a realistic laser driver, the injected charge spectrum (Fig 7.(d)) exhibits multiple injection positions. The higher energy electrons are injected 1 mm after ct_1 , when a_0 has dropped to 2.5, and contribute to the high energy peak centered on 632 MeV in Fig. 6.(b). The lower energy peak at 466 MeV in Fig. 6.(b) is composed of electrons trapped at different positions: 1 mm after ct_1 and at ct_2 , which explains why this peak (Index 1 of Figs. 6.(b) and (c)) has a relatively higher energy spread than peak 1 for Gaussian driver (Table I).

The dynamics of electron injection results from the evolution of the laser and plasma cavity. Snapshots of the first plasma cavity behind the laser pulse are shown for the Gaussian driver in Fig. 7.(e) and (g), and for a realistic driver in Fig. 7.(f) and (h), at $ct_1 = 1800 \mu\text{m}$ and $ct_2 = 4000 \mu\text{m}$ respectively. At ct_1 , for the ideal Gaussian laser simulation, injection of electrons on axis has just begun in a perfectly symmetric bubble, while for the realistic case most of the already injected electrons are greatly defocused and spread from -30 to $30 \mu\text{m}$. The accelerating fields are similar for Fig. 7.(e) and (f). However, in the realistic case, electrons ionized early are desynchronized with the trapping portion of the bubble due to off axis laser fluence fluctuations resulting in a $3 \mu\text{m}$ shorter bubble compared to the Gaussian case. This prevents continuous injection and the generation of electrons with energy above 700 MeV [Fig. 6.(a) and (b)].

Comparison of the two cavity structures at ct_2 (Fig. 7 (g) and (h)), provides insight on the effects of transverse asymmetry evolution on the acceleration process.

In the ideal Gaussian laser case, most of the initially injected charge is accelerated, and the injection process remains continuous.

The transverse centroid variations and stronger defocusing with the realistic laser profile induce important losses throughout the interaction process, which enables trapping of up to 10 pC around ct_2 , in an off-axis bubble with half of the accelerating maximum compared to a Gaussian cylindrically symmetric driver.

Laser and electron beam positions in the xOz transverse plane are plotted in Fig. 8 as functions of the po-

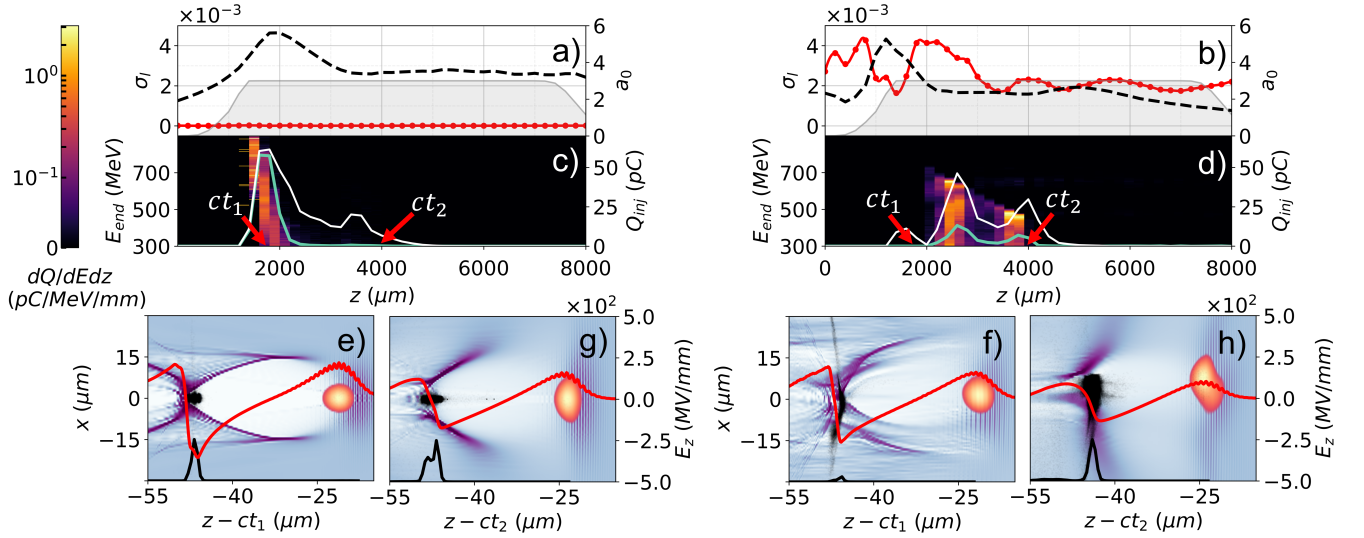


FIG. 7 : Simulated evolution of laser pulse and electron bunch characteristics for the ideal Gaussian laser profile (columns on the left) and the realistic laser field profile [columns on the right]. Panels (a) and (b): laser asymmetry function σ_l (red dots) and spline approximated asymmetry function curve (red curve) as functions of position on the propagation axis; peak normalized laser potential a_0 (black dashed-line), and normalized longitudinal unperturbed plasma density profile (grey area). Panels (c) and (d): injected charge Q_{inj} (vertical axis on the right) as function of position (all electrons plotted as a white line, and angularly selected ± 3 mrad electrons as green line); The panels (c) and (d) also show the spectral charge density $dQ/dE_{end}dz$ of electrons (black-red-yellow colormap) with final energy E_{end} for the angular selection as a function of the injection position z . Panels (e) and (g) [(f) and (h) for the simulation with realistic laser field]: transverse slice of the normalized charge density perturbation ρ/en_0 on the $z-x$ plane at $ct_1 = 1800 \mu\text{m}$ and resp. $ct_2 = 4000 \mu\text{m}$; in these panels the electron macro-particles positions are shown as small black dots (with their size pondered by their individual charge). Superposed in these panels is the laser driver intensity's normalized envelope (orange colormap); in the same panels, the black and red lines correspond respectively to the density and the longitudinal electric field E_z on the axis of maximum laser intensity.

sition along the propagation axis in vacuum. The ideal Gaussian laser trajectory is centered on the laser axis in vacuum, closely followed by the electron beam trajectory. The electron beam transverse size remains relatively constant in the plasma and grows symmetrically around $x = 0$ after plasma exit. For a realistic laser driver, the laser trajectory [Fig. 8.(b)] in vacuum oscillates around the $x = 0$ axis. Self-focusing in the plasma lowers the amplitude of the displacement off-axis (compare red line and black dashed line).

After electron trapping, $z > 2000 \mu\text{m}$, the electron bunch trajectory is centered on the laser centroid, and its standard deviation reaches up to $10 \mu\text{m}$. This behavior clearly demonstrates the impact of the asymmetry of the transverse laser driver on the pointing of the electron beam at the exit of the plasma.

C. Charge fluctuations due to laser intensity distribution

Simulations were performed to analyze the effects of variations of the intensity profile on the resulting charge. The laser electric field was reconstructed for 3 reference profiles with the modified GSA algorithm described in Appendix A and the remaining simulation input parameters are the same as in Fig. 6.(b) (reported in section

IV A). The density was varied between 1.7×10^{18} and $2.3 \times 10^{18} \text{ cm}^{-3}$.

To characterize the laser energy distribution for each profile, we define the following effective energy ratio :

$$E_{ratio} = \frac{1}{N_z} \sum_{z=-z_R}^{+z_R} \frac{\int_{r=0}^{r_{eff}} \int_{\theta=0}^{2\pi} r dr d\theta F(r, \theta, z)}{\int_{r=0}^{r_{max}} \int_{\theta=0}^{2\pi} r dr d\theta F(r, \theta, z)}, \quad (5)$$

with z being the propagation position of the laser with respect to z_f , N_z the number of evenly spaced positions z used to perform the summation in the Rayleigh range $[-z_R, \dots, 0, \dots, z_R]$ and $F(r, \theta, z)$ the fluence at each propagation position in vacuum. The integral origin is defined as the position of the fluence maximum. This ratio quantifies the average effective energy in the characteristic divergence boundaries $[-z_R, z_R]$ of the laser propagation axis, and within an area of radius r_{eff} . Improving this ratio increases the portion of energy usable for the injection of electrons.

The total accelerated charge Q is calculated within the whole $E - \theta_x$ space and plotted in Fig. 9 as a function of n_0 for the 3 laser profiles and densities ranging from 1.7 to $2.3 \times 10^{18} \text{ cm}^{-3}$. In this regime, within the chosen set of parameters, the total charge Q remains lower than the theoretical value calculated for a matched laser for most of the input densities n_0 . This is a consequence of the non-Gaussian laser transverse distributions, and

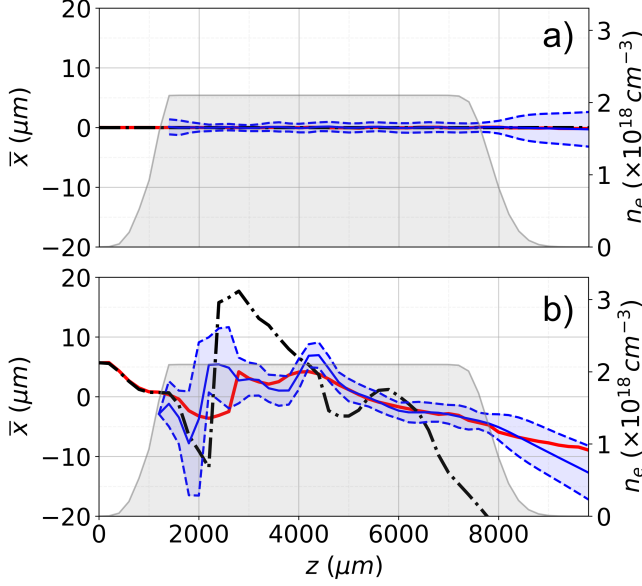


FIG. 8 : Laser beam (solid red line) and electron bunch (solid blue line) positions in the xOz plane for (a) Gaussian case and (b) Laguerre-Gauss case. The blue dashed lines are the \pm RMS σ_x size of the selected bunch. The laser position is defined as the centroid of the fluence distribution in an area of radius r_{eff} around the fluence maximum. For reference, the dash-dotted black line represents the position of the laser beam in vacuum and the grey area is the longitudinal density profile (right-end side vertical axis scale).

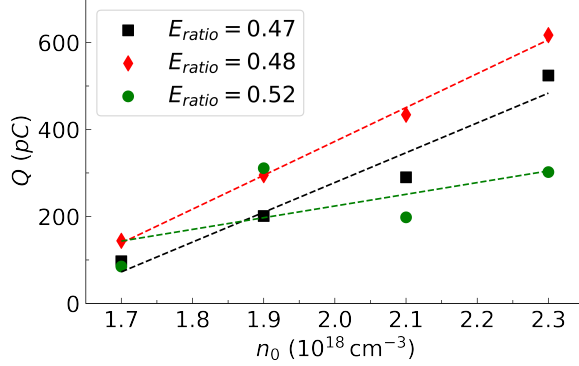


FIG. 9 : Total injected bunch charge Q for 3 different simulated laser profiles as a function of n_0 . For each profile, the corresponding E_{ratio} is calculated by eq. (5), setting $N_z = 21$: black squares profile with $E_{ratio} = 0.47$ - red diamonds profile with $E_{ratio} = 0.48$ - green circles profile with $E_{ratio} = 0.52$. For each profile, the dashed curve is the linear regression of the data points.

of the fact that the laser spot size is not matched with the bubble radius. Comparing the 3 values simulated for $n_0 = 2.1 \times 10^{18} \text{ cm}^{-3}$, while E_{ratio} fluctuates between 0.47 and 0.52, the total charge Q varies from 198 to 434 pC. A relative effective energy fluctuation $\delta E_{ratio}/E_{ratio} = 5\%$ leads to a relative charge fluctu-

ation $\delta Q/Q = 38\%$. For the laser profile resulting in the highest total charge, i.e. $E_{ratio} = 0.48$, increasing the density n_0 from 1.9×10^{18} to $2.1 \times 10^{18} \text{ cm}^{-3}$ increases Q from 295 to 434 pC. A relative density fluctuation of 5% leads to a relative charge fluctuation $\delta Q/Q = 19\%$. This shows that taking into account small errors either on the gas density value or on the calculated effective energy ratio leads to significant charge fluctuations, of the same order of magnitude as the one measured experimentally (Fig. 3).

The averaged calculated charge measured within the same boundaries as experimental data is 113 pC ($\bar{Q}_{tot} = 95 \text{ pC}$ in experiment), with an RMS relative charge fluctuation of 56% ($\delta \bar{Q}_{tot}/\bar{Q}_{tot} = 47\%$ in experiment). There is a good agreement between the average simulated and experimental charge for the same central density $\bar{n}_0 = 2.2 \times 10^{18} \text{ cm}^{-3}$. In conclusion, this analysis shows that improving the quality and the stability of the laser energy distribution and the stability of the plasma density are crucial to achieve stable and high-energy, high charge electron spectra.

V. CONCLUSIONS

Experiments were carried out during the commissioning phase in the long focal area of the APOLLON laser facility, to study the influence of the laser beam properties on the quality of electron beams generated by ionization injection and laser wakefield acceleration in a gas cell. A detailed analysis of the laser beam in the transverse plane was performed using fluence measurements in the focal volume. Particle in Cell simulations were performed with a reconstruction of the laser field obtained from the measured laser fluence map as input, leading to electron spectra in close agreement with experimental results, for the accelerated charge, energy distribution and pointing of the electron beam at the exit of the plasma. The presented results also show that this degree of quantitative agreement can be found without using computationally demanding full 3D simulations.

These high fidelity simulations rely on the calculation of the laser electric field from experimental data providing the fluence at different positions along the propagation in vacuum.

An iterative method based on a modified version of the Gerchberg-Saxton algorithm [22], which allows the reconstruction of a realistic laser electric field based on a collection of fluence images in vacuum (Fig. 4), was used. The implementation of asymmetric laser drivers leads to better agreement of the simulation output bunch characteristics to measured experimental data in comparison to simulations using a perfect Gaussian driver (Fig. 6 and Table I).

These realistic simulations highlight the effects of laser field spatial characteristics (centroid fluctuations and asymmetry quantified by σ_l) on the injection and acceleration of the electrons (Fig. 7 and Fig. 8). The symmetry

degradation from a Gaussian laser driver leads to a loss of both peak energy and total accelerated bunch charge (Table I), which could be mitigated through optimization of the gas cell density characteristics.

The impact of shot-to-shot fluctuations of the laser transverse distribution and of plasma density on the accelerated bunch charge, have been quantified and the source of charge fluctuations in experiments identified. The stabilization of these fluctuations would lead to an improved stability of the produced electron spectra.

ACKNOWLEDGMENTS

We acknowledge the resources and assistance of the computing center MesoLUM managed by ISMO (UMR8214) and LPGP (UMR8578), University Paris-Saclay (France). Experimental results were achieved using APOLLON Research Infrastructure and we gratefully acknowledge the work of the Laboratoire pour l'Utilisation des Lasers Intenses (UMR7605) staff during planning and execution of the experiment. APOLLON facility was partially funded by Equipex Cilex (Centre interdisciplinaire lumière extrême) grant N° ANR-10-EQPX-25-01, and by region Ile-de-France.

Appendix A: Modified Gerchberg-Saxton algorithm (GSA) to model the laser driver

In the experimental campaign described in this work, only the fluence maps $F(x, y, z)$ of the laser pulse at specific distances z_k , with $k = 0, 1, \dots, k_{\max}$ from the focal spot were measured.

A Gaussian temporal profile was assumed for the laser pulse, with the measured FWHM duration in intensity τ_{FWHM} . Under this hypothesis, the linear relation between the peak fluence F_0 and peak intensity I_0 is :

$$F_0 = \frac{\tau_{FWHM}}{2} \sqrt{\frac{\pi}{\log 2}} I_0. \quad (A1)$$

Given this linear relation between fluence $F(x, y, z)$ and intensity $I(x, y, z)$, an electric field at position z can be defined from a phase map $\psi(x, y)$ and a fluence $F(x, y, z)$:

$$\begin{aligned} E(x, y, z) &= E[F(x, y, z), \psi(x, y)] = \\ &= \sqrt{I(x, y, z)} \exp\{i\psi(x, y)\}. \end{aligned} \quad (A2)$$

To initialize the realistic PIC simulations of this work, a reconstruction of the laser electric field at a given plane was necessary. Since only the fluence (and thus intensity) maps at multiple planes were known experimentally, to reconstruct the laser electric field using Eq. A2 the field phase map had to be reconstructed.

For this purpose, a modified implementation of the Gerchberg-Saxton algorithm (GSA) [22] was used to find the field phase $\psi(x, y)$ at z_0 and thus the laser electric

field $E_{GSA, z_0}(x, y, z_0) = E[F(x, y, z_0), \psi(x, y)]$, from the available data on the the fluence $F(x, y, z_0)$ at z_0 and other planes, each referred to as z_k .

In the following a simplified description of the field reconstruction algorithm used in this work is reported.

This version of the GSA aims at finding a reconstruction of the laser field at z_0 through an expansion in Hermite-Gauss (HG) modes [23], using the measured $F(x, y, z_k)$ fluence maps. Since the propagation of the HG modes $HG_{n,p}$ at z_k is analytically known, this reconstruction is equivalent to finding the estimated HG expansion coefficients $D_{n,p}$ (and thus the corresponding field phase map). The indices n, p denote the order of the HG mode along the x, y axis respectively.

At each iteration $iter$ of the algorithm, the estimated expansion in HG modes is propagated from the position z_0 to $z_{k_{\max}}$, with an improvement of the estimate at each of the intermediate positions z_k . This update of the estimated coefficients for the HG expansion uses the estimated coefficients from the previous measurement plane at z_{k-1} and the measured fluences $F(x, y, z_k)$. As in the original GSA formulation [22], the estimated propagated phase is combined with the fluence at the measurement planes in the calculations.

After one iteration ends, the procedure is repeated starting from z_0 , using the coefficients (and thus the phase map) estimated from the previous iteration.

The implementation of the modified GSA used for this work can be described by the following pseudocode:

- Find an initial estimate of the coefficients $D_{n,p}$ projecting the intensity corresponding to the fluence $F(x, y, z_0)$ on the $HG_{n,p}(x, y, z_0)$ modes at z_0 . In the following we denote the projection of a function $f(x, y, z)$ on the HG modes with the notation Proj:

$$D_{n,p} = \text{Proj}[f(x, y, z), HG_{n,p}(x, y, z)]. \quad (A3)$$

- For $iter = 0 \rightarrow N_{\text{iter}}$ and for $k = 0 \rightarrow k_{\max}$:
 - define the propagated field as

$$E_{GSA, z_k}(x, y, z_k) = \sum_{n,p} D_{n,p} \cdot HG_{n,p}(x, y, z_k); \quad (A4)$$

- find the phase map ψ as:

$$\psi(x, y) = \arg(E_{GSA, z_k}(x, y, z_k)); \quad (A5)$$

- combine the measured fluence $F(x, y, z_k)$ with the phase $\psi(x, y)$ to find the function E'_{GSA, z_k} using Eq. A2:

$$E'_{GSA, z_k}(x, y, z_k) = E[F(x, y, z_k), \psi(x, y)]; \quad (A6)$$

- combine the previous estimate of the HG coefficients with those obtained from the projection of E'_{GSA, z_k} on the HG modes at z_k :

$$\begin{aligned} D_{n,p} &= (1 - \alpha) \cdot D_{n,p} + \\ &+ \alpha \cdot \text{Proj}[E'_{GSA, z_k}, HG_{n,p}(x, y, z_k)]; \end{aligned} \quad (A7)$$

For this work the number of iterations was chosen as $N_{\text{iter}} = 10$. The coefficient α for the weighted sum of the previous and new HG expansion coefficients are chosen in order to obtain convergence.

Once the algorithm has performed the iterations passing through the measurements planes, using Eq. A2 the estimated field phase $\psi(x, y)$ can be easily found and combined with the measured fluence $F(x, y, z_0)$ of the laser to reconstruct its field $E_{GSA, z_0}(x, y, z_0) = E[F(x, y, z_0), \psi(x, y)]$.

In this algorithm, the mentioned projection of a func-

tion $f(x, y, z_k)$ on the HG modes at z_k was defined as:

$$\begin{aligned} & \text{Proj}[f(x, y, z_k), \text{HG}_{n,p}(x, y, z_k)] = \\ & = \int_{-\Delta X/2}^{\Delta X/2} \int_{-\Delta Y/2}^{\Delta Y/2} dx dy f(x, y, z_k) \times \\ & \quad \times \text{HG}_{n,p}^*(x, y, z_k), \end{aligned} \quad (\text{A8})$$

where $(\Delta X, \Delta Y)$ are the data rectangular grid length along each axis. The HG modes at z_k are defined also using the origins $(x_{0,k}, y_{0,k})$ and the projection waists $w_{0x,y}$. The latter are set sufficiently small to make the Hermite-Gauss modes decay within the projection integral boundaries, and sufficiently large to fit the part of the transverse intensity map further away from the origin. The values of $(x_{0,k}, y_{0,k})$ are optimized to improve the quality of the laser field reconstruction, as will be described in a future work.

The field reconstruction obtained with described phase retrieval algorithm would be sufficient to initialize the laser pulse in a realistic PIC simulation in 3D Cartesian geometry. However, for the simulations in quasi-3D geometry [21] of this work, which use a cylindrical grid, a further decomposition in Laguerre-Gauss modes is necessary, as described in Section III B.

-
- [1] T. Tajima and J. M. Dawson, Phys. Rev. Lett. **43**, 267 (1979).
 - [2] E. Esarey, C. Schroeder, and W. Leemans, Reviews of modern physics **81**, 1229 (2009).
 - [3] F. S. Tsung, R. Narang, W. B. Mori, C. Joshi, R. Fonseca, and L. O. Silva, Physical Review Letters **93**, 185002 (2004).
 - [4] S. Corde, C. Thaury, A. Lifschitz, G. Lambert, K. Ta Phuoc, X. Davoine, R. Lehe, D. Douillet, A. Rousse, and V. Malka, Nature Communications **4**, 1 (2013).
 - [5] M. Chen, E. Esarey, C. Schroeder, C. Geddes, and W. Leemans, Physics of Plasmas **19**, 033101 (2012).
 - [6] C. McGuffey, A. Thomas, W. Schumaker, T. Matsuoka, V. Chvykov, F. Dollar, G. Kalintchenko, V. Yanovsky, A. Maksimchuk, K. Krushelnick, *et al.*, Physical Review Letters **104**, 025004 (2010).
 - [7] A. Pak, K. Marsh, S. Martins, W. Lu, W. Mori, and C. Joshi, Physical Review Letters **104**, 025003 (2010).
 - [8] M. Mirzaie, S. Li, M. Zeng, N. Hafz, M. Chen, G. Li, Q. Zhu, H. Liao, T. Sokollik, F. Liu, *et al.*, Scientific reports **5**, 1 (2015).
 - [9] A. Pukhov and J. Meyer-ter Vehn, Applied Physics B **74**, 355 (2002).
 - [10] I. Kostyukov, E. Nerush, A. Pukhov, and V. Seredov, Physical review letters **103**, 175003 (2009).
 - [11] F. Massimo, A. Beck, J. Dérouillat, I. Zemzemi, and A. Specka, Physical Review E **102**, 033204 (2020).
 - [12] C. K. Birdsall and A. B. Langdon, *Plasma Physics via Computer Simulation* (Taylor and Francis Group, 2004).
 - [13] B. Beaurepaire, A. Vernier, M. Bocoum, F. Böhle, A. Jullien, J.-P. Rousseau, T. Lefrou, D. Douillet, G. Iaquaniello, R. Lopez-Martens, A. Lifschitz, and J. Faure, Phys. Rev. X **5**, 031012 (2015).
 - [14] J. Ferri, X. Davoine, S. Fourmaux, J. Kieffer, S. Corde, K. T. Phuoc, and A. Lifschitz, Scientific reports **6**, 1 (2016).
 - [15] L. T. Dickson, C. I. D. Underwood, F. Filippi, R. J. Shalloo, J. B. Svensson, D. Guénot, K. Svendsen, I. Moulancier, S. D. Dufrénoy, C. D. Murphy, N. C. Lopes, P. P. Rajeev, Z. Najmudin, G. Cantono, A. Persson, O. Lundh, G. Maynard, M. J. V. Streeter, and B. Cros, Phys. Rev. Accel. Beams **25**, 101301 (2022).
 - [16] W. Leemans, A. Gonsalves, H.-S. Mao, K. Nakamura, C. Benedetti, C. Schroeder, C. Tóth, J. Daniels, D. Mittelberger, S. Bulanov, *et al.*, Physical review letters **113**, 245002 (2014).
 - [17] A. Popp, J. Vieira, J. Osterhoff, Z. Major, R. Hörlein, M. Fuchs, R. Weingartner, T. Rowlands-Rees, M. Marti, R. Fonseca, *et al.*, Physical review letters **105**, 215001 (2010).
 - [18] D. Papadopoulos, J. Zou, C. Le Blanc, G. Chériaux, P. Georges, F. Druon, G. Mennerat, P. Ramirez, L. Martin, A. Fréneaux, *et al.*, High Power Laser Science and Engineering **4** (2016).
 - [19] T. Audet, P. Lee, G. Maynard, S. D. Dufrénoy, A. Maitrallain, M. Bougeard, P. Monot, and B. Cros, Nuclear Instruments and Methods in Physics Research Section A: Accelerators, Spectrometers, Detectors and Associated Equipment **909**, 383 (2018).
 - [20] R. Lehe, M. Kirchen, I. A. Andriyash, B. B. Godfrey, and J.-L. Vay, Computer Physics Communications **203**, 66 (2016).
 - [21] A. Lifschitz, X. Davoine, E. Lefebvre, J. Faure, C. Rechatin, and V. Malka, Journal of Computational Physics **228**, 1803 (2009).

- [22] R. W. Gerchberg, *Optik* **35**, 237 (1972).
- [23] F. Pampaloni and J. Enderlein, arXiv preprint physics/0410021 (2004).
- [24] W. Lu, M. Tzoufras, C. Joshi, F. Tsung, W. Mori, J. Vieira, R. Fonseca, and L. Silva, *Physical Review Special Topics-Accelerators and Beams* **10**, 061301 (2007).